GEOSPHERE

THE GEOLOGICAL SOCIETY OF AMERICA®

Photogrammetric digital outcrop reconstruction, visualization with textured surfaces, and three-dimensional structural analysis and modeling: Innovative methodologies applied to fault-related dolomitization (Vajont Limestone, Southern Alps, Italy)

Andrea Bistacchi[1], Fabrizio Balsamo[2], Fabrizio Storti[2], Mahtab Mozafari[3], Rudy Swennen[3], John Solum[4], Christian Tueckmantel[4], and Conxita Taberner[4]

[1]Department of Earth and Environmental Sciences, Università degli Studi di Milano Bicocca, Piazza della Scienza 4, 20126 Milano, Italy
[2]Dipartimento di Fisica e Scienze della Terra Macedonio Melloni, Università degli Studi di Parma, Parco Area delle Scienze, 7/A, 43124 Parma, Italy
[3]Division of Geology, Katholieke Universiteit Leuven, Celestijnenlaan 200 E, 3001 Heverlee, Belgium
[4]Carbonate Research, Integrated Geoscience Department, Shell Global Solutions International B.V., Kesslerpark 1, 2288 GS Rijswijk (ZH), The Netherlands

ABSTRACT

Different remote sensing technologies, including photogrammetry and LIDAR (light detection and ranging), allow collecting three-dimensional (3D) data sets that can be used to create 3D digital representations of outcrop surfaces, called digital outcrop models (DOM). The main advantages of photogrammetry over LIDAR are represented by the very simple and lightweight field equipment (a digital camera), and by the arbitrary spatial resolution, that can be increased simply getting closer to the outcrop or by using a different lens. The quality of photogrammetric data sets obtained with structure from motion (SFM) techniques has shown a tremendous improvement over the past few years, and this is becoming one of the more effective ways to collect DOM data sets. The Vajont Gorge (Belluno Dolomites, Italy) provides spectacular outcrops of jurassic limestones (Vajont Limestone Formation) in which mesozoic faults and fracture corridors are continuously exposed. Some of these faults acted as conduits for fluids, resulting in structurally controlled dolomitization. A 3D DOM study, based on a photogrammetric SFM data set, was carried out, aimed at enabling interdisciplinary characterization and reconstruction of coupled brittle deformation and fluid flow processes. For this study we used a DOM (730 m × 360 m × 270 m) consisting of continuous triangulated surfaces representing the outcrop, textured with high-resolution images. Interpretation and modeling performed on this data set include (1) georeferencing of structural measurements and sampling stations; (2) tracing of stratigraphic boundaries, structural surfaces, and dolomitization fronts (ground-truthed); (3) correlation and extrapolation of realistic 3D surfaces from these traces; and (4) development of a 3D geological model at the scale of the Vajont Gorge, including stratigraphy, faults, dolomitization fronts, and volumetric meshes suitable for the statistical analysis of structural, diagenetic, and geochemical parameters. The DOM study highlighted the close relationship between faults and dolostone geobodies, demonstrating that dolomitization was guided by fluid infiltration along Mesozoic normal faults. In order to explore the uncertainty associated with the 3D model of irregularly shaped dolostone bodies, three different 3D dolostone geobody realizations have been modeled, providing a minimum, intermediate, and maximum estimate of the dolostone/limestone volumetric facies ratio, while honoring the field constraints.

1. INTRODUCTION

Many geological characterization projects have included the reconstruction of quantitative three-dimensional (3D) representations of suitable outcrops, called digital outcrop models (DOMs; Bellian, 2005) or virtual outcrops (McCaffrey et al., 2005). This was allowed by the widespread availability of technologies like DGPS (with submeter precision; Maerten et al., 2001; Xu et al., 2001; Pearce et al., 2006; Smith et al., 2013), laser scanning (LIDAR—light detection and ranging, and TLS—terrestrial laser scanner; Bellian, 2005; White and Jones, 2008; Buckley et al., 2008; Hodgetts, 2013), and close-range photogrammetry (Dueholm and Olsen, 1993; Lebel et al., 2001; Haneberg, 2008; Vasuki et al., 2014; Tavani et al., 2014). DOMs allow significant advances in field data collection and interpretation for four main reasons (e.g., Hodgetts, 2013): (1) they allow for a detailed quantitative description of the geometry and spatial relationships of geological objects; (2) they allow for collection of large volumes of data, homogeneously distributed on outcrops, providing a sound statistical base for modeling; (3) they allow for unified analysis of very large outcrops, sometimes at reservoir scale; and (4) they allow for 3D exploration of outcrops, with suitable software, under various points of views, with the possibility to navigate around the model, sometimes resulting in different interpretations than the more limited and static view that a geologist can have by studying only the accessible parts of outcrops.

A DOM workflow can be subdivided into three main phases: (1) collection of topography and images of the outcrop, (2) processing and output of a DOM in suitable formats, and (3) geological interpretation and modeling. Each of these phases can be completed with alternative techniques and software, as described in the following.

DGPS was possibly the first technology used to collect precisely georeferenced geological data, particularly in structural geology. For example, it has been applied to fluvio-deltaic sediments (Xu et al., 2001), folds (Pearce et al., 2006), fault networks (Maerten et al., 2001), ductile shear zones (Pennacchioni and Mancktelow, 2007) and, more recently, to the collection of scanlines across large fault zones, allowing quantitative characterization of fault zone architecture (Smith et al., 2013) and hydraulic properties (Bistacchi et al., 2013). This technique is very well suited to obtain the precise location of structural measurements or sampling stations (Smith et al., 2013), but is very time consuming if the goal is to map continuous structures, for example bedding or fault traces. Moreover, it is limited by the accessibility of outcrops (e.g., it is not possible to perform this kind of survey on vertical walls). For this reason, most projects at present are based on a remote sensing approach, with the collection of 3D image data with LIDAR or photogrammetry. In this case, the geological interpretation is carried out a posteriori on a workstation using suitable software (similar to seismic data interpretation), but it can be also combined and quality-checked with data collected in the field using traditional techniques (e.g., qualitative sketches, structural measurements, samples).

Laser scanning data sets consist of 3D point clouds collected by a laser device capable of measuring the X, Y, and Z coordinates of objects (outcrop surfaces) hit by the laser beam. TLS used in the field generally have a range of <1 km and a spatial resolution of 1–5 cm (Vosselman and Maas, 2010). In a typical LIDAR workflow, the 3D point cloud could be colorized by collecting photos with a calibrated camera attached to the scanner, thus associating an RGB (red-green-blue) value from a photo to each point in the point cloud. This provides photorealistic point clouds (White and Jones, 2008; Kurz et al., 2012), but it must be noted that the spatial resolution of such photorealistic point clouds is limited by the resolution of the coarser data set (either the photos or point cloud depending on survey conditions; see discussion herein). LIDAR surveys have been successfully applied to numerous projects dealing with a large number of different geological structures (e.g., Trinks et al., 2005; Candela et al., 2009; Lovely et al., 2010; Bistacchi et al., 2011; Kurz et al., 2012).

Close-range photogrammetry techniques allow for obtaining the same kind of data sets collected from LIDAR, with the advantage of overcoming some of their limitations, as well as providing the benefit of requiring only a simple digital camera. The advantages associated with this approach are summarized here and discussed in more detail in the following. The main advantage is an arbitrary spatial resolution, which can be increased simply by moving closer to the outcrop or by using longer focal length lenses (e.g., Bistacchi et al., 2011). A second advantage is the perfect alignment between the point cloud and the images, since the point cloud is actually obtained from the images. In this way, the point cloud is natively colorized, and it allows for the generation of high-quality triangulated surfaces textured with image data (with the techniques discussed in the following). The required equipment is very light and can be easily used even in difficult field conditions. This approach allowed the acquisition of 3D images of individual millimeter-thick fault traces with a 0.5 mm spatial resolution (Bistacchi et al., 2011). Possible problems and disadvantages of photogrammetry with respect to LIDAR include accuracy control (which can be solved using highly redundant data sets, addressed in the following), and time-consuming processing (which can be solved with increasingly powerful workstations and optimized software).

Regardless of the selected 3D outcrop reconstruction technique, either LIDAR or photogrammetry, the output is a point cloud data set. This can be used as it is in the geological interpretation (e.g., White and Jones, 2008), or a triangulated surface representing the outcrop surface can be generated from the point cloud. In order to obtain a photorealistic surface, this must be textured with image data (basically, a small portion of an image is assigned to each triangle in the surface, and passed to the graphic card for visualization). This kind of visualization is very common in computer graphics (e.g., in architectural applications or videogames), but not in geology. With only a few exceptions (e.g., Tavani et al., 2014), geological digital elevation models are textured with aerial orthophotos, which do not allow representation of details on almost vertical, or even overhanging, rock walls. In any case, texturing is generally performed with images that have a significantly reduced resolution (e.g., Tavani et al., 2014). However, in this contribution we present an innovative workflow that allows outcrop surfaces to be textured with the original images collected in the field, without any loss of resolution and/or resampling.

The interpretation of DOMs can be performed either using generic laser scanning or photogrammetry surveying software (e.g., RIEGL RiSCAN, www.riegl.com; CloudCompare, www.cloudcompare.net), which generally do not provide specific geological tools, or using more specialized geological packages. Some of these (e.g., Coltop3D, www.coltop3d.ch) focus on the interpretation of point clouds in terms of fracture surfaces. However, to perform a more general geological interpretation (i.e., including stratigraphy, structure, and other elements), a good option would be a geomodeling package like Skua-Gocad (www.pdgm.com/products/skua-gocad), Move (www.mve.com/software/move), or Petrel (www.software.slb.com). There are no direct standard ways to import DOMs in these packages. In the following, we present our solution to import the DOM in Skua-Gocad and then perform the interpretation and modeling in this environment.

The project discussed here was carried out in the Vajont Gorge (Veneto and Friuli Venezia Giulia, Italian Southern Alps), which provides spectacular outcrops of carbonate-dominated sequences where fault zones and/or fracture corridors are well exposed on vertical walls. Some of these fault zones provided fluid pathways, resulting in structurally controlled dolomitization of the Vajont Limestone, associated with a very high porosity increase (e.g., Zempolich and Hardie, 1997; Ronchi et al., 2012). Although previous studies (Zempolich and Hardie, 1997) have shown that dolomitization is controlled by faulting, no detailed structural data were provided to associate dolomitization with a particular fault kinematic setting or tectonic event and, hence, to a particular stage in

the complex tectonic evolution of this part of the Alps, which includes a rifting and a passive margin stage, overprinted by the Dinaric and Alpine orogenies.

We present here the workflow that allowed us to build the DOM of the Vajont Gorge with photogrammetry, and show how the stratigraphic and structural interpretation was carried out, and how dolostone was mapped on the walls of the gorge. We then present a methodology allowing us to model the complex geometries of dolostone geobodies, affected by relevant uncertainty, and discuss how this workflow allowed the highlighting of the relationships between faulting and dolomitization.

■ 2. GEOLOGICAL OUTLINE OF THE VAJONT GORGE AREA

The Vajont Gorge was carved by the Vajont River in the Jurassic–Cretaceous carbonate-dominated sequence of the Belluno Dolomites (Fig. 1) in the eastern Southern Alps, which represent the retrowedge of the Alpine belt, where contractional deformation driven by continental collision developed from the Neogene to the Present (Dal Piaz et al., 2003). The Vajont Limestone (late Bajocian–Bathonian) forms a large part of the walls of the Vajont Gorge and is the target of this study. This formation is 350–400 m thick and is composed of whitish to grayish reworked oolitic limestones in thick beds that are locally dolomitized (Zempolich and Hardie, 1997). These reworked platform sediments are interpreted to be derived from the Friuli Platform, at the northern edge of the Adriatic Platform, in Jurassic and Cretaceous time (Masetti et al., 2012), and resedimented by gravity-flow processes on the slope connecting the Friuli Platform with the Belluno Basin (Bosellini and Masetti, 1972).

The Vajont Valley coincides with the core of a composite fold resulting from the interference between the east-west–trending Erto syncline (Ferasin, 1956; Riva et al., 1990) and the north-south–trending Massalezza syncline (Massironi et al., 2013). These folds are kinematically related to north-south– and east-west–trending Oligocene to Miocene contractional to transcurrent fault systems (e.g., Riva et al., 1990; Doglioni, 1992b; Castellarin and Cantelli, 2000; Massironi et al., 2013; Chistolini et al., 2014), which define a fault block corresponding to the project area (Fig. 1).

Extensional Pre-Alpine Mesozoic faults are present in the study area (Doglioni, 1990). At the regional scale, the traces of these structures are discontinuous due to the fragmentation caused by the Tertiary tectonics. For this reason it is difficult to map the real extent of the Mesozoic fault systems and to define their age, which is generally assumed to be Middle Jurassic (e.g., Doglioni, 1992a).

Dolomitization of the Vajont Limestone is associated with a very high porosity, as high as 25%; this contrasts with the very low porosity of the original limestone (<2%; Zempolich and Hardie, 1997). Previous studies (Zempolich and Hardie, 1997) showed that the dolomitization here is controlled by faults; however, no detailed structural data were provided relating dolomitization to a particular fault kinematic or tectonic phase, and therefore to a particular stage in the complex evolution of this part of the Alps, an evolution that includes a rifting stage, a passive margin stage, and two orogenic stages. This is one of the reasons why the DOM study has been undertaken.
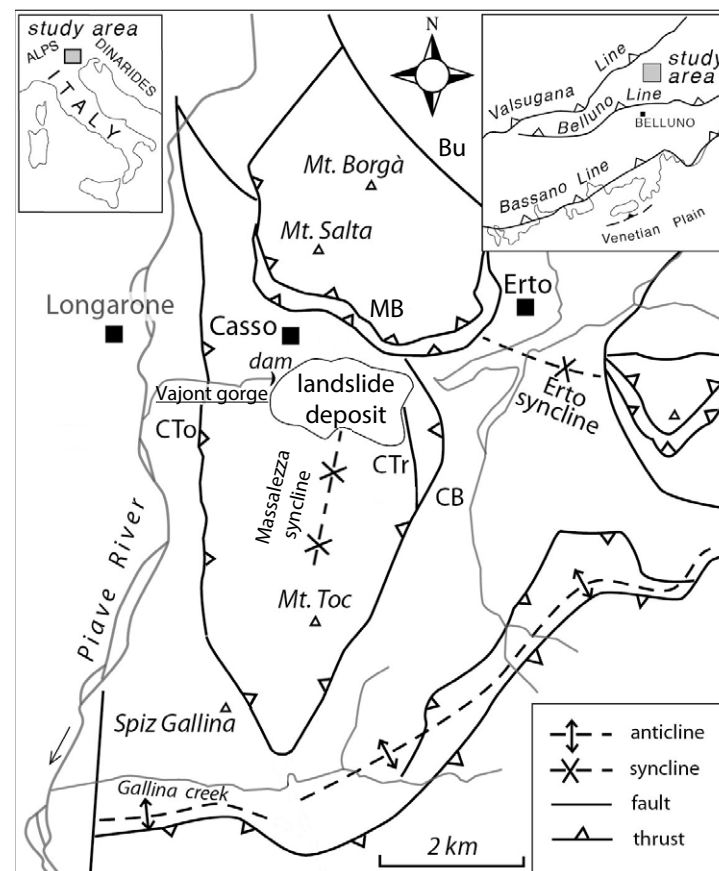

Figure 1. Tectonic sketch map and location of the study area in the Belluno Dolomites (modified after Riva et al., 1990; Massironi et al., 2013). MB—Monte Borgà thrust; Bu—Canalone Buscada fault; CB—Croda Bianca fault; CTr—Col Tramontin fault; CTo—Col delle Tosatte fault (note that Massironi et al., 2013, in contrast with others, showed that this is an east-dipping thrust fault). Landslide deposit is the 1963 Vajont rockslide accumulation. Insets show location of the study area (gray box) in the Southern Alps.

2.1. Structural Framework of the Vajont Gorge

The large-scale 3D structural analysis developed with the DOM workflow described in the following was based on preliminary results of mesoscale structural analyses. These analyses were carried out on outcrops on both sides of the Vajont Gorge, and in some tunnels in its north side, excavated for the construction and maintenance of the Vajont dam. While an exhaustive description of the structural analysis results is not possible here, we note some key observations to help in understanding some choices in the DOM project.

Bedding orientation in the Vajont Limestone is fairly constant, with average of 082/19 (dip azimuth/dip convention) with a very limited scatter (Fig. 2A). Multiple fault sets are present in the gorge, mostly extensional fault zones (Fig. 2B) and minor contractional (Fig. 2C) and strike-slip (Fig. 2D) deformation structures. Extensional structures are interpreted as Mesozoic, while contractional and strike-slip ones are interpreted as Tertiary (Massironi et al., 2013).

Extensional (Ext) preorogenic fault zones can be subdivided into three sets: Ext1 (average attitude 212/65), Ext2 (332/61), and Ext3 (265/70). Set Ext3 is undersampled in the stereoplot shown in Figure 2B, obtained by traditional measurements on accessible outcrops (roads and tunnels). However, we show that this set is important on the Vajont Gorge walls, particularly in the higher part of the north wall. Detecting this fault set in nonaccessible parts of the outcrops was an important result of the photogrammetric study.

Where fault zones belonging to the extensional sets affect dolostone bodies, they are characterized by cataclasites and fault breccias cemented by dolomite (Fig. 2) or by slickensides decorated by dolomite fibers; therefore,

the fault zones are coeval and kinematically compatible with dolomite veins (average attitude 261/88; Fig. 2). Dolomite veins are also present in limestones, at distances of as much as 10–20 m from dolostone bodies. In limestones at larger distances from the dolostone bodies, cataclasites, slickensides and veins are cemented with calcite.

Tertiary orogenic strike-slip and thrust fault zones can be classified as thrust set 1 (Thr1, 115/22), thrust set 2 (Thr2, 183/76), right-lateral strike-slip fault zones (RL, 200/79), and left-lateral strike-slip fault zones (LL, 261/84) (Figs. 2C, 2D). Given the similar orientation, RL and LL probably represent fault zones and/or fractures belonging to the extensional preorogenic sets Ext1 and Ext3, reactivated under tertiary contractional stress fields. However, this kind of reactivation is not common in the Vajont Gorge, and most extensional fault zones show well-preserved extensional kinematic indicators. It is significant that all the contractional and strike-slip deformation structures are associated with calcite cement, fibers, and veins, both in limestones and in dolostone, pointing to fluids with a different composition with respect to those (Mg-rich) associated with the extensional deformation structures.
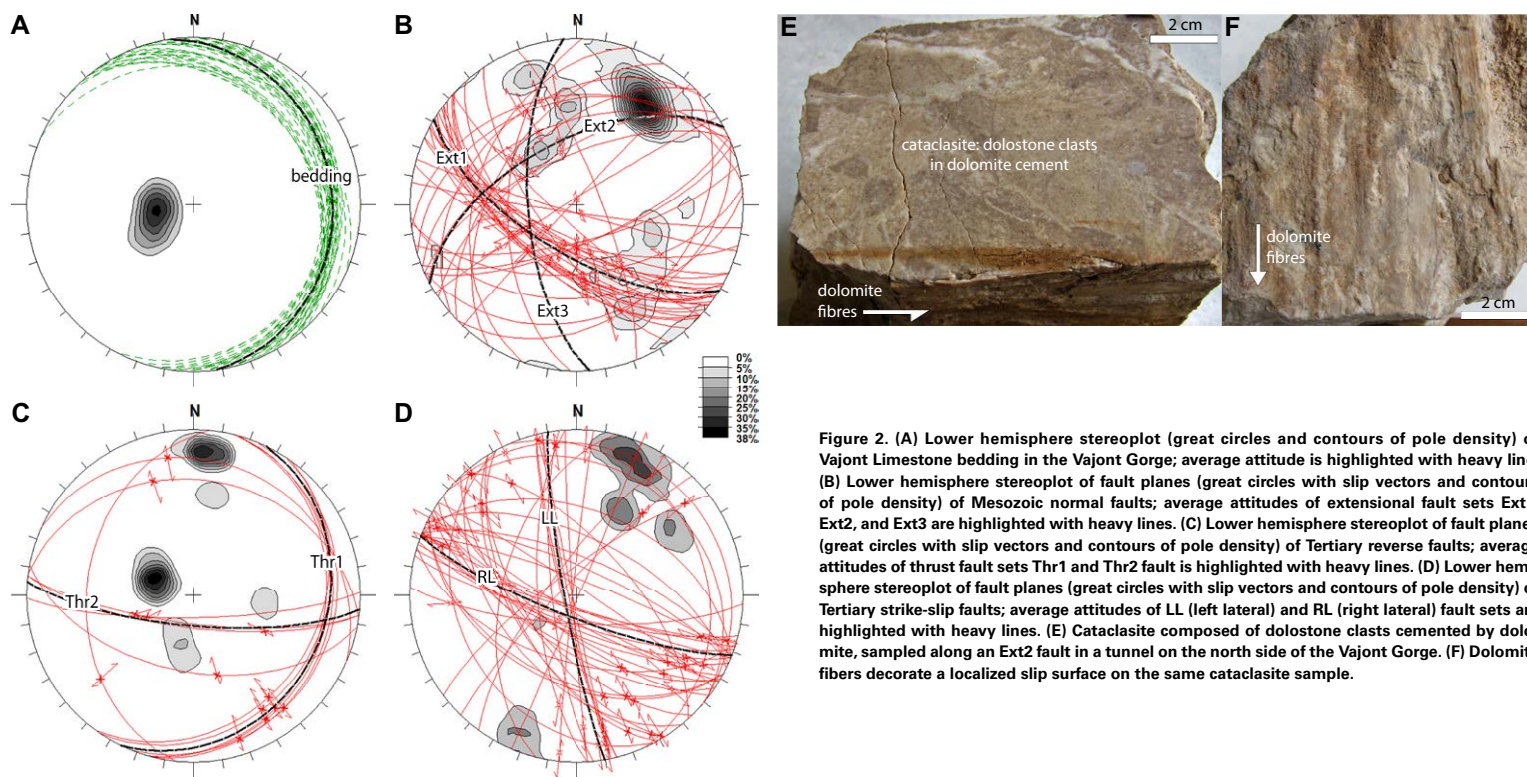

Figure 2. (A) Lower hemisphere stereoplot (great circles and contours of pole density) of Vajont Limestone bedding in the Vajont Gorge; average attitude is highlighted with heavy line. (B) Lower hemisphere stereoplot of fault planes (great circles with slip vectors and contours of pole density) of Mesozoic normal faults; average attitudes of extensional fault sets Ext1, Ext2, and Ext3 are highlighted with heavy lines. (C) Lower hemisphere stereoplot of fault planes (great circles with slip vectors and contours of pole density) of Tertiary reverse faults; average attitudes of thrust fault sets Thr1 and Thr2 fault is highlighted with heavy lines. (D) Lower hemisphere stereoplot of fault planes (great circles with slip vectors and contours of pole density) of Tertiary strike-slip faults; average attitudes of LL (left lateral) and RL (right lateral) fault sets are highlighted with heavy lines. (E) Cataclasite composed of dolostone clasts cemented by dolomite, sampled along an Ext2 fault in a tunnel on the north side of the Vajont Gorge. (F) Dolomite fibers decorate a localized slip surface on the same cataclasite sample.

■ 3. BUILDING THE VAJONT GORGE DIGITAL OUTCROP MODEL

We summarize here the main principles behind close-range photogrammetry, particularly in the structure from motion (SFM) implementation. We explain how the data set was collected and processed in the Vajont Gorge project and show how this data set was used to generate a DOM of the gorge based on triangulated surfaces textured with the same images collected in the field, with no loss of resolution.
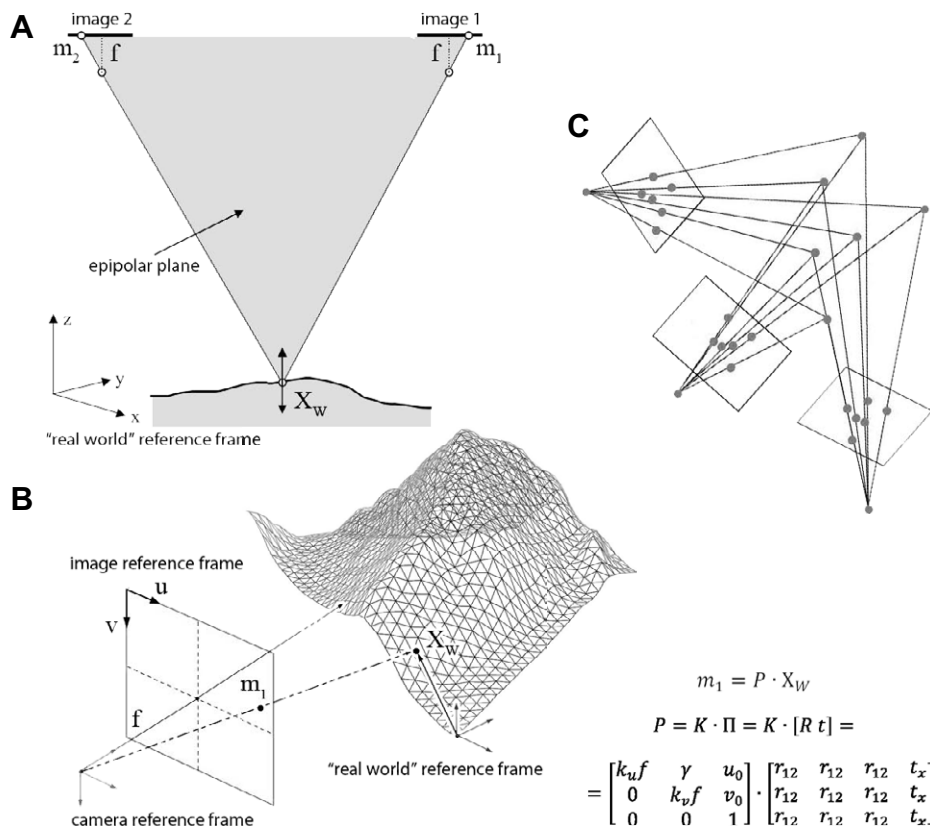
3.1. Principles of Photogrammetry and SFM

Photogrammetry may be defined as the sum of techniques allowing quantitative measurements and reconstruction of the geometry of solid objects to be carried out from photos and other image data. It is a branch of remote sensing that was traditionally developed as a fundamental tool in geodesy and topography, but has broad application beyond these fields (Lillesand et al., 2008).

The basic principle in photogrammetry is that of stereoscopic viewing, which is used to obtain 3D coordinates of points identified in a pair of images (stereocouple). If some parameters are known about the internal geometry and optics of the cameras, and about the position of the cameras in 3D space, the 3D position of an object seen in both images can be calculated by means of triangulation on the epipolar plane (Fig. 3A). These parameters define the image orientation and are subdivided into exterior orientation parameters (position of camera in 3D space) and interior orientation parameters (geometry and optics of the camera). Image orientation parameters define, for each image, the projection transformation between the real world 3D space and the 2D image plane, allowing the transformation of the coordinates of an object in 3D space to coordinates of its image in the 2D image plane and vice versa. The simplest possible projection transformation is based on the idealized pinhole camera model (Fig. 3B), which can be applied to cameras with no lenses or with completely distortion-free lenses. This projection can be also used if images are corrected for lens distortion (Tsai, 1987).

Traditional photogrammetric workflows are based on pairs of photos (stereocouples), and in this case all the interior and exterior orientation parameters must be known a priori. However, a novel approach has been developed that allows the use of large redundant collections (bundles) of images (Fig. 3), taken from different positions and even with different cameras, to obtain the interior and exterior orientation parameters from the images. This approach, SFM, was originally developed in the framework of robotic vision (Hartley and Zisserman, 2004), and was further developed for phototourism projects (Snavely et al., 2006).

The idea behind the SFM approach is simple. Given a set of several images shot from different positions, if in every image several points can be recognized (expressed in image coordinates) representing the same real world features (the same X, Y, Z positions), then we can build a large system of equations from the projection equations associated with the images and invert the system to obtain both the interior and exterior orientation matrices of each image and the X, Y, Z coordinates of the features. The oriented photos are processed almost as in the stereocouple workflow to get the final point cloud (e.g., Lillesand et al., 2008). This approach, although computationally intensive, has been found to be very effective in building large photogrammetric models in architectural and archaeological applications (Wu, 2013). Our study of the Vajont Gorge is one of the first applications of the SFM approach in structural geology. An important advantage of this method, compared with the traditional stereocouple workflow, is that each feature is defined from a redundant number of photos (Snavely et al., 2006) and error estimates are just another output from model inversion. This ensures a high quality of the results

$$m_1 = P \cdot X_W$$

$$P = K \cdot \Pi = K \cdot [R\ t] =$$

$$= \begin{bmatrix} k_u f & \gamma & u_0 \\ 0 & k_v f & v_0 \\ 0 & 0 & 1 \end{bmatrix} \cdot \begin{bmatrix} r_{12} & r_{12} & r_{12} & t_x \\ r_{12} & r_{12} & r_{12} & t_x \\ r_{12} & r_{12} & r_{12} & t_x \end{bmatrix}$$

Figure 3. (A) Triangulation of a point $X_W = [X\ Y\ Z\ 1]^T$ on the Earth's surface from a pair of oriented photos shot with a camera with focal length f; m_1 and m_2 are the images of the object X_W on images 1 and 2, respectively. (B) The pin-hole projection defined as $m_1 = P \cdot X_W$. The three-dimensional (3D) point X_W is projected to the image point $m_1 = [u_1\ v_1\ 1]^T$ along a line originating from the optical center of the camera. The position and orientation of the camera reference frame are defined by the external orientation matrix $\Pi = [R\ t]$. Position vectors in the image plane are expressed in image coordinates [$u\ v$] and depend from the interior orientation parameters matrix K, in turn depending from the focal length f, principal point [$u_0\ v_0$] γ, and number of pixels per unit distance in image coordinates [$k_u\ k_v$]. Additional parameters, omitted here, may be added to the interior orientation parameters matrix K to account for lens distortion (Tsai, 1987). (C) Redundant triangulation in a structure from motion bundle of images.

because points with precision lower than a given threshold are automatically rejected by the inversion algorithm.

An SFM workflow involves the following steps: (1) automatic recognition of distinctive features in each image; (2) automatic recognition of common features within all images; (3) solution of the projection equation system and output of X, Y, Z coordinates of features (called sparse point cloud) and camera interior and/or exterior orientation; (4) processing of the oriented photos to obtain a colorized dense point cloud. The last step generally includes the removal of spherical distortion from the images, which are saved as undistorted photos.

Bundler (Snavely et al., 2006) and VSFM (Wu, 2013) are extensively tested open-source packages for steps 1–3. The output from both Bundler and VSFM can be processed with CMVS/PMVS2 (Furukawa and Ponce, 2010) in order to complete the workflow with step 4. Bundler is of more common use (e.g., in archaeology), while VSFM is highly optimized for running on specific graphics processing units (GPU). Other open-source or freeware packages are available (e.g., MicMac, www.micmac.ign.fr), and the commercial software Agisoft Photoscan (www.agisoft.com; used by Tavani et al., 2014) provides a user-friendly graphical user interface based on Bundler. However, due to limitations in the output formats and in the size of the model, the latter packages do not allow for completion of the workflow described here. Another possibility for SFM processing is to use web services where photos are uploaded and remotely processed (e.g., Microsoft Photosynth, https://photosynth.net/).

3.2. Data Collection and Processing in the Vajont Gorge

The Vajont Gorge data set is composed of 1753 photos shot with a Nikon D700 camera, with a full-frame, 36 × 23.9 mm, 12.1 megapixel, CMOS (complementary metal-oxide semiconductor image sensor), characterized by a particularly good signal-to-noise ratio at ISO 200 (e.g., www.clarkvision.com/articles/digital.sensor.performance.summary/#SNR). The photos were acquired as NEF (Nikon raw electronic format) 14-bit raw files. Multiple lenses were used in order to obtain a data set including both lower resolution panoramic views and higher detail close-up images. The lenses that were used are a superwide-angle Nikkor AF-S 14–24 mm f/2.8G ED, a general-purpose Nikkor AF-S 24–120 mm f/3.5–5.6 G IF VR, and a telephoto Nikkor AF-S VR 70–300mm f/4.5–5.6G IF-ED.

The 1753 photos were shot from 63 stations, 714 images (from 34 stations) looking toward the north side of the Vajont Gorge and 1039 images (from 29 stations) looking toward the south side. To ensure consistent light conditions and minimize shadows projected from the rim of the gorge, all photos of the north side were shot in the evening, almost at sunset, when no direct sunlight comes into the gorge. Under these conditions light is low and the high sensitivity of our camera was very useful. A similar condition was achieved for the south side, shooting all photos in less than an hour in the early morning.

After all the photos were collected, distorted photomosaics were quickly generated and used to collect annotations in the field for reference during in-terpretation (Fig. 4). This is very useful; in this way, results of the discussion carried out on the outcrops with all members of the project team can be transferred very easily into the 3D interpretation.

Georeferencing of the Vajont Gorge DOM is based on targets distributed on both sides of the gorge. The X, Y, Z coordinates of each target were measured with a Topcon GTS-4B total station. This time-consuming topographic workflow was necessary because GPS measurements are not reliable in the deep and narrow Vajont Gorge. The connection to the external reference frame, represented by the national Gauss-Boaga grid, was achieved by measuring a landmark on the top of the Vajont Dam and another landmark on the tower of a church in Longarone. The baseline provided by these 2 points is ~2.2 km long, providing a very good alignment. The X and Y coordinates used in the project were obtained by removing the first three digits from Gauss-Boaga coordinates. This transformation was applied in order to reduce the number of significant digits in the DOM and 3D models, allowing (1) a better precision in single-precision calculations and (2) a reduction of file size for all objects, allowing, for example, a more fluid visualization on the workstation screen.

Before running the SFM software, it is necessary to select the photos to be included in the processing (some low-quality photos were rejected for this study) and to convert these photos from NEF to JPG format. High-quality almost lossless JPG is preferred to, e.g., PNG for large projects in order to reduce the total file size. In this project the photos were then divided into four different sets, one for the north side of the gorge and three for the south side. Subdividing the south side in three sets was necessary because the overlap between the three subsets is limited due to the unfavorable distribution of shooting stations on the north side, and so it would have been not possible or very difficult for the SFM software to match photos across these subsets. The SFM processing was performed with Bundler (Snavely et al., 2006) and CMVS/PMVS2 (Furukawa and Ponce, 2010). The output includes (1) a set of dense point clouds, which were eventually merged into a single final point cloud; (2) undistorted photos, i.e., images corrected for camera lens distortion, that conform to the simplified pin-hole camera model; and (3) interior and exterior orientation matrices for each photo.

Each point cloud was georeferenced using CloudCompare (www.danielgm.net/cc/), which allows for georeferencing the point clouds and also provides the rotation-translation-scaling matrix associated with this transformation. To apply the same transformation to the camera orientation matrices, a custom Matlab (www.mathworks.com) application was used. The accuracy of this transformation is critical when texturing the triangulated surfaces with the original images. The output point cloud covers a volume of ~730 m × 360 m × 270 m.

3.3. Implementation of a DOM Based on Textured Triangulated Surfaces

The main difference between the traditional DOM workflow and the one adopted in this project is that outcrops here are represented by triangulated surfaces textured with the original images using a pin-hole projection. Tra-
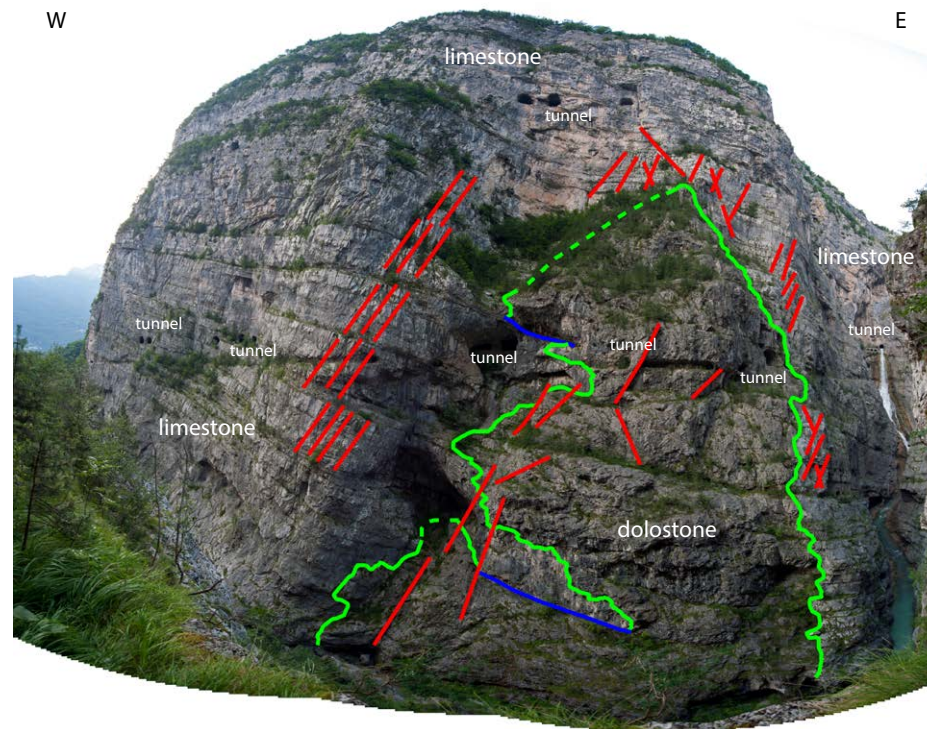
Figure 4. Example of a distorted photomosaic with annotations drawn directly in the field. The dolostone body boundaries have been classified as boundaries along bedding surfaces (blue), boundaries along faults (red), and replacement fronts not related to other structures (green). Windows of tunnels cited in text are highlighted. Scale varies a great deal in this distorted panoramic view.

ditional DOM workflows are based on point clouds, or on triangulated surfaces textured with low-resolution images, resulting in a degradation of image quality. In order to obtain this kind of representation, we first generated the triangulated outcrop surface from the photogrammetric point cloud, and then performed the projection from each image plane to the DOM surface. This is possible using a LIDAR point cloud; however, when texturing with the original high-resolution images a perfect alignment of images is required, which is more easily obtained in a photogrammetry workflow.

Meshing of the point cloud to obtain the outcrop surface was performed with a Poisson surface reconstruction algorithm (Kazhdan et al., 2006) implemented in Meshlab (meshlab.sourceforge.net). This method allows for easy meshing of very dense point clouds, controlling the output mesh resolution with various parameters, provided that a surface normal vector (pointing toward the camera or laser scanner) is defined for each point. This allows for variable resolution meshes with increased detail where the outcrop surface shows more variability and larger triangles where outcrops are smoother. The output surface was then translated into the Gocad ASCII format by means of a custom Matlab toolbox.

In order to apply the original high-resolution photos as textures to the DOM surface, image coordinates (u and v coordinates measured in each

image plane) must be projected on each vertex of the outcrop triangulated surface (Fig. 5). This has been performed using the pin-hole projection transformation (Fig. 3B) implemented in the custom Matlab toolbox. Using this projection is possible because the images are undistorted (spherical aberration corrected) in the photogrammetric workflow, at the step where the dense point cloud is generated. One of the strengths of our approach is the use of the same transformation to generate the 3D geometry of the outcrops and project the images, which guarantees the internal consistency of the resulting DOM.

When modeling a complex 3D object, different portions of its surface are best represented in different images. For this reason, the DOM surface was divided into different portions, each one associated with a particular image (Fig. 5). Because the 1753 photos covering the Vajont Gorge outcrops are highly redundant, a selection was performed to find the minimum subset of photos that were useful. This selection was performed on two image subsets: images collected with the ultrawide-angle 14 mm lens, and images collected at higher magnification (generally between 24 and 50 mm focal length), thus providing a lighter (less dense) data set, suitable for most applications, and a heavier one with the highest resolution.
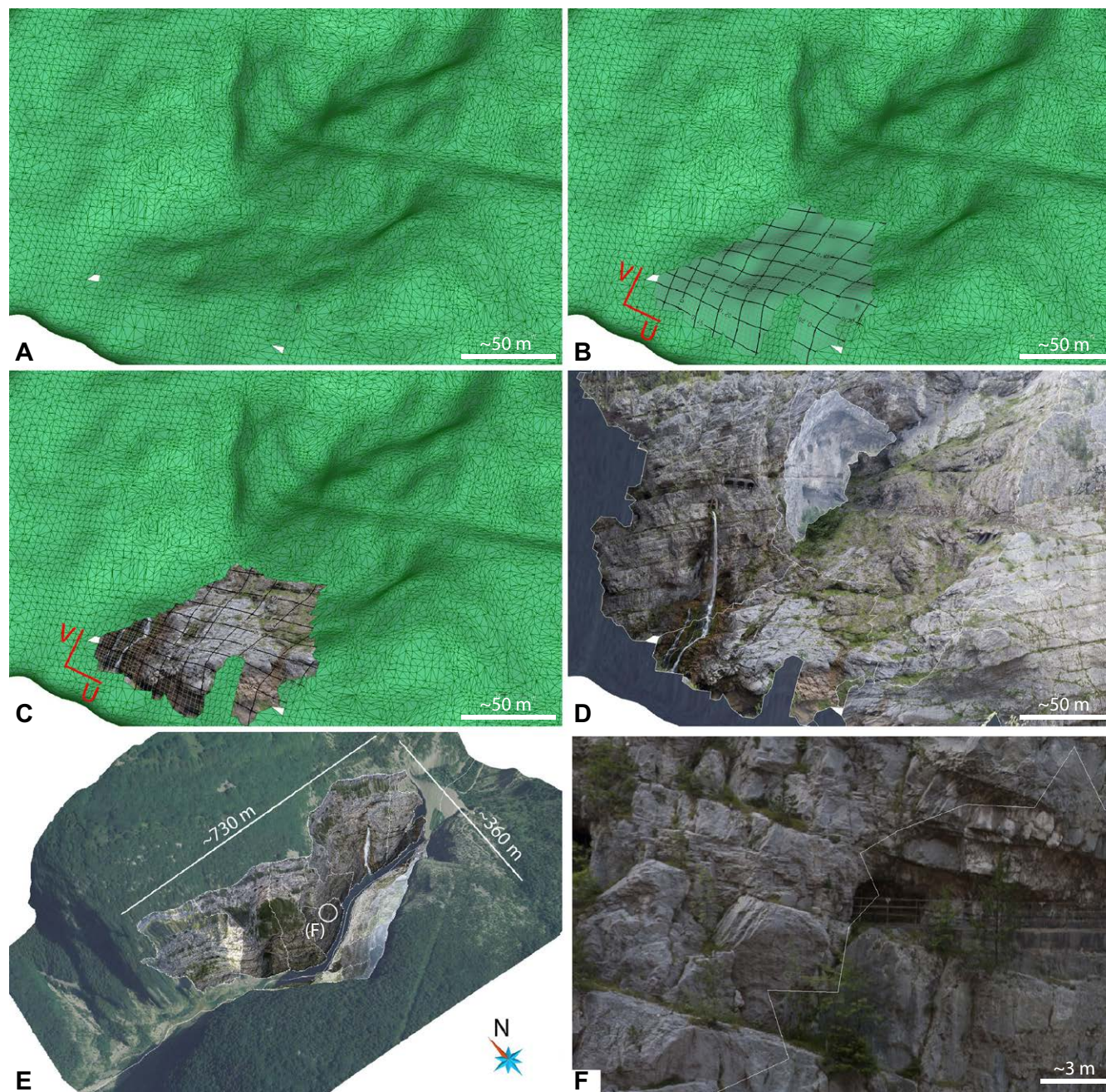
Bistacchi et al. | Digital outcrop model study of fault-related dolomitization in the Vajont Limestone

To view the 3D interactive version of Figure 5E, please visit www.unimib.it/geo3d.

Figure 5. (A) Triangulated digital outcrop model (DOM) surface obtained with Poisson interpolation from the structure from motion (SFM) point cloud. (B) The [u v] image coordinates are shown on a portion of the DOM corresponding to one photo captured in the field. (C) The photo is used, at the original resolution, to texture the DOM portion shown in B. (D) DOM surface textured with multiple images; each one is attributed to a different portion of the triangulated surface (thin white lines). Whitish rocks are limestones, brownish rocks are dolostones. (E) Overview of the Vajont Gorge: portions of DOM textured with individual images (lower resolution data set, 14 mm focal length) are highlighted with white lines. DOM is ~730 m × 360 m × 270 m. A triangulated surface obtained from aerial LIDAR (light detection and ranging) data, textured with an aerial orthophoto, is added out of the area covered by our high-resolution photogrammetric survey. To view the 3D interactive version of Figure 5E, please visit www.unimib.it/geo3d. (F) Detail of the DOM on the north side of the Vajont Gorge (location in E). Two images from the intermediate resolution data set (24 mm focal length) are shown. Note the very good match between adjoining images.

After the selection was done, each portion of the outcrop was associated with one of the selected images. Each portion was extracted from the overall outcrop surface and saved as an individual surface in Gocad ASCII format using the custom Matlab toolbox. This allows visualizing a DOM composed of several triangulated surfaces, each one associated with an undistorted image retaining the original resolution (Fig. 5). The resulting data set is suitable for visualization and interpretation in geomodeling packages, including the Skua-Gocad suite.

This workflow results in a much higher resolution data set with respect to any previous reported achievement. For example, in Tavani et al. (2014) the triangulated surfaces were textured with single low-resolution 4096 × 4096 pixel images (16 megapixels), while in this study the digital outcrop model is textured with >100 4256 × 2832 pixel images (12 megapixel × 100 = 1.2 gigapixel), retaining the resolution of original images. The resolution in the Vajont Gorge case is as great as a 2 cm/pixel, much higher than in most LIDAR projects covering a similar area.

Another relevant difference with previous projects is that the interpretation is performed directly in Skua-Gocad, while others perform it in external software (e.g., OpenPlot; Tavani et al., 2014) and then import the results in geomodeling packages.

■ 4. WORKFLOW FOR INTERPRETATION AND MODELING OF STRATIGRAPHY, FAULTS, AND DOLOSTONE GEOBODIES

Here we outline the workflow used in the interpretation of the Vajont Gorge DOM performed directly in Skua-Gocad. The first step of the interpretation consisted of transferring to the DOM the interpretation recorded in the field on printed distorted photomosaics (Fig. 4). By digitizing in 3D on high-resolution images, being able to zoom in and fully exploit the centimeter-scale resolution, we were able to improve the precision of the interpretation carried out in the field. In addition to fault traces, we digitized the traces of dolostone body boundaries (Fig. 6). These can be easily recognized in the field and in photos, because dolostone and limestone show different weathering color, morphology, and fracturing style; the dolostone is brownish, rounded, and affected by less systematic fractures, while limestone is whitish-grayish, shows well-defined bedding, and is more fractured. We have classified the dolostone body boundaries as boundaries along bedding surfaces, boundaries along fault zones, and replacement fronts not related to other deformation or sedimentary structures (Figs. 4 and 6). After having classified the walls of the Vajont Gorge as limestone versus dolostone, a facies proportion analysis was performed:

To view the 3D interactive version of Figure 6, please visit www.unimib.it/geo3d.
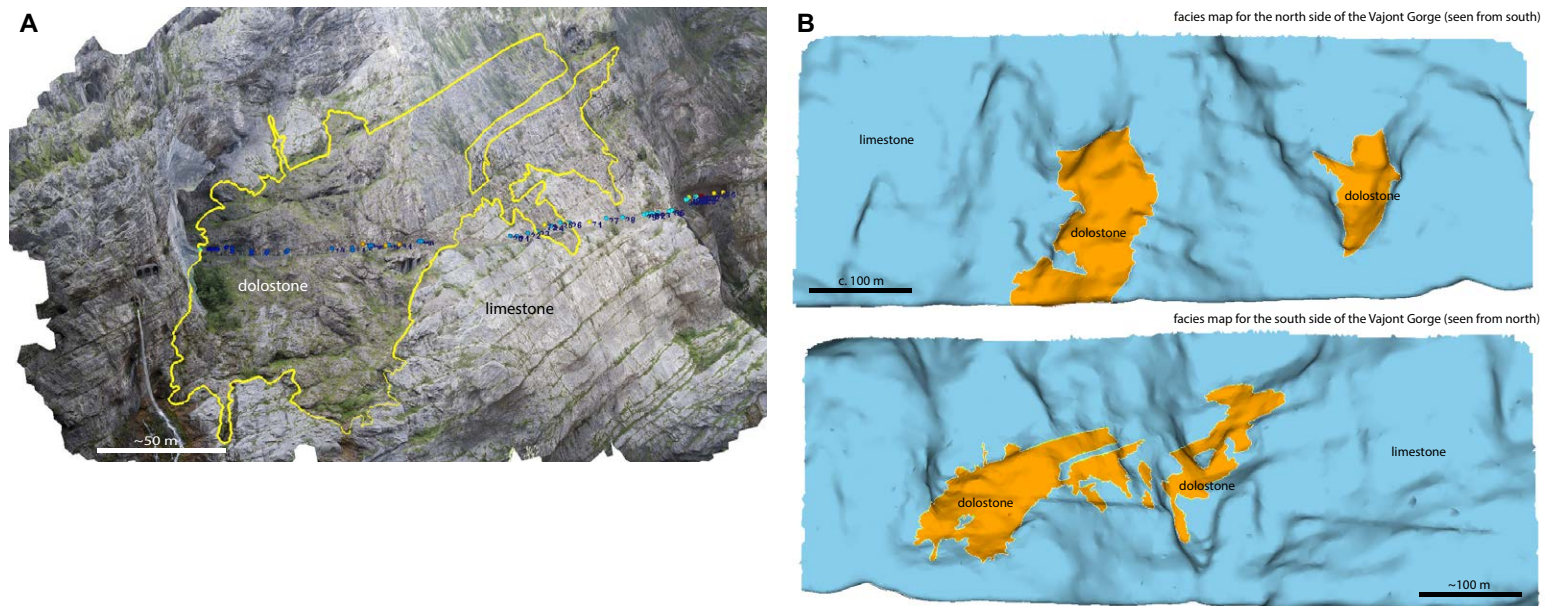

Figure 6. (A) Traces of dolostone bodies digitized onto the digital outcrop model (DOM) and the locations of samples collected on the south side of the gorge. (B) DOM surfaces classified as limestone versus dolostone (and dolomitized limestone): the dolostone and dolomitized limestones cover 11% and 10% of the outcrops on the north and south walls, respectively (Table 1). To view the 3D interactive version of Figure 6, please visit www.unimib.it/geo3d.

the dolostones and dolomitized limestones (transition facies) cover 11% and 10% of the outcrops on the north and south walls, respectively (Fig. 6; Table 1). At this stage, other information collected in the field, such as sampling locations, was transferred to the 3D model (Fig. 6) and allowed to quality check the interpretation. We were also able to digitize the traces of two tunnels in the subsurface of the north side of the Vajont Gorge (Fig. 7), where detailed structural analyses were carried out. This was possible because windows along these tunnels are visible on the DOM (Fig. 4). Tunnels were particularly useful in the modeling because the boundaries of some dolostone bodies are well exposed along them, allowing for better definition of their 3D geometry.

A second step in the interpretation consisted of reconstructing the local stratigraphy by correlating and digitizing 12 bedding surfaces that are particularly prominent and distinctive on both sides of the gorge (Fig. 8) and thus provide fundamental markers for calculating fault displacement values. This task was complicated by the fact that bedding is obliterated by the dolomitization process.

Given these difficulties, this task was completed using a closed loop correlation strategy on the two walls of the Vajont Gorge, supported by virtual wells defined on selected sections (Fig. 8). At least one virtual well was defined for each nondolomitized portion, allowing detailed measurement of bed thicknesses, and highlighting of features like smaller beds arranged in particularly distinctive patterns. Comparing the logs in virtual wells allowed for correlation across dolomitized sections. Because the Vajont Gorge is extremely narrow and its upper and lower ends are not dolomitized, the consistency of this kind of correlation can be checked by demonstrating that it can be consistently followed along a closed loop, e.g., along the north face from east to west, crossing the west end of the gorge to the south face, along the south face from west to east, and back to the north face crossing the east end (Fig. 8). Bedding traces and virtual well markers have been interpolated with an implicit surface approach (Frank et al., 2007), then slightly smoothed with DSI (discrete smooth interpolator, implemented in Skua-Gocad; Mallet, 2002).

Figure 7. Two perspective views of the tunnels in the subsurface of the north side of the Vajont Gorge. The digital outcrop model is sliced and rotated in order to see the tunnels in the subsurface.

The final products of the bedding interpretation exercise are continuous triangulated surfaces representing 12 bedding surfaces that were interpolated in the Vajont Gorge area; these surfaces extend from one side of the gorge to the other, and extend in the subsurface to the north and to the south (Fig. 8).

The interpretation of faults was performed directly in 3D using a custom Gocad wizard that allows the user to interactively create planar rectangular surfaces with specified length, height, and attitude, centered at a single point picked on the DOM (Fig. 9). In this way it is very easy to adjust the geometry of these objects to fault and fracture traces observed on the Vajont Gorge walls. In cases of ambiguous attitude (e.g., when the geometry of a fault trace allows different interpretations), this part of the analysis was cross-checked with results from the mesoscale structural analysis (summarized herein). Moreover, where mutual crosscutting or termination of one fault on another one has been detected in the DOM, these relationships have been replicated in the 3D fault surfaces (Fig. 9).

Modeling of 3D dolostone bodies was not as straightforward as for stratigraphy or faults, because these bodies show very complex, irregular, and convolute shapes (Fig. 6). For this part of the modeling, which is associated with a varying degree of uncertainty (see discussion following), we tested two different methodologies (workflows A and B). The input objects for the two workflows are the same, i.e., traces of dolostone body boundaries digitized on the DOM, and interpreted dolostone body boundary lines that have been digitized on the 12 interpolated bedding surfaces. Constraints for this interpretation are the relationships with faults and with traces of dolostone body boundaries digitized on the DOM and in tunnels. These constraints are quite stringent in some cases, but in other cases the uncertainty is high. For this reason three scenarios have been generated that result in a minimum, intermediate, and maximum predicted volume of dolomitized limestone.

TABLE 1. FACIES PROPORTIONS ON THE NORTH
AND SOUTH WALLS OF THE VAJONT GORGE

Digital outcrop model surface	Facies	Three-dimensional area (m²)	Proportion (%)
North wall	total	239333	100.00
	dolostone	26335	11.00
	limestone	212998	89.00
South wall	total	257673	100.00
	dolostone	24952	9.68
	limestone	232721	90.32
North-south average	total	497006	100.00
	dolostone	51287	10.32
	limestone	445719	89.68

Bistacchi et al. | Digital outcrop model study of fault-related dolomitization in the Vajont Limestone

Figure 8. (A) Traces of selected bedding surfaces digitized onto the digital outcrop model (DOM). Markers corresponding to these surfaces have been added to virtual wells to facilitate correlation between different parts of the Vajont Gorge. (B) Graphical representation of the closed loop correlation strategy applied to the north and south walls and across dolostone bodies. (C) Interpolated bedding surfaces. Scale varies in these three-dimensional views. To view the 3D interactive version of Figure 8, please visit www.unimib.it/geo3d.

A

730 m

B

C

Workflow A is based on a traditional explicit reconstruction of complex surfaces as a sum of simpler surface parts, and is based on the following steps.

1. Traces of dolostone body boundaries digitized on the DOM were cut in distinct sections at intersections with bedding surfaces.

2. Interpreted dolostone body boundary lines that were digitized on the bedding surfaces were cut in distinct sections at intersections with the DOM surfaces.

3. Using the traces of dolostone body boundaries digitized on the DOM and those digitized on the bedding surfaces, closed pseudorectangular frames were established, and within each frame a triangulated surface was generated.

4. All these individual surfaces, which are perfectly connected at common edges, were collected and merged in a single surface representing a first approximation of the dolostone body boundary.

5. The single surface representing each dolostone body boundary was smoothed and interpolated with DSI (Mallet, 2002), using the traces of dolostone body boundaries digitized on the DOM as constraints, to obtain the final geometries shown in Figure 10.

6. The surfaces representing the dolostone body boundaries can be used to generate other representations, e.g., regular voxets suitable for exporting to different geomodeling packages.

Workflow B is based on the extraction of implicit surfaces as isosurfaces of a scalar lithology property interpolated on a volumetric tetrahedral mesh (Frank et al., 2007), and is based on the following steps.

1. Using the dolostone body boundary lines digitized on outcrops, a lithology property was generated on outcrop surfaces, with values of 1 = limestone, 2 = transition, and 3 = dolostone.

2. Using dolostone body boundary lines digitized on bedding surfaces, a lithology property was generated on each bedding surface, with values of 1 = limestone, 2 = transition, and 3 = dolostone. Given the uncertainty in dolostone distribution on bedding surfaces, particularly at increasing distance from the outcrops, three different properties (called lithology_min, lithology_med, lithology_max), representing three different scenarios, were generated.

3. The lithology property for each scenario (lithology_min, lithology_med, lithology_max) was interpolated on a tetrahedral volume comprising all the model volume, using the bedding and outcrop surfaces as constraints.
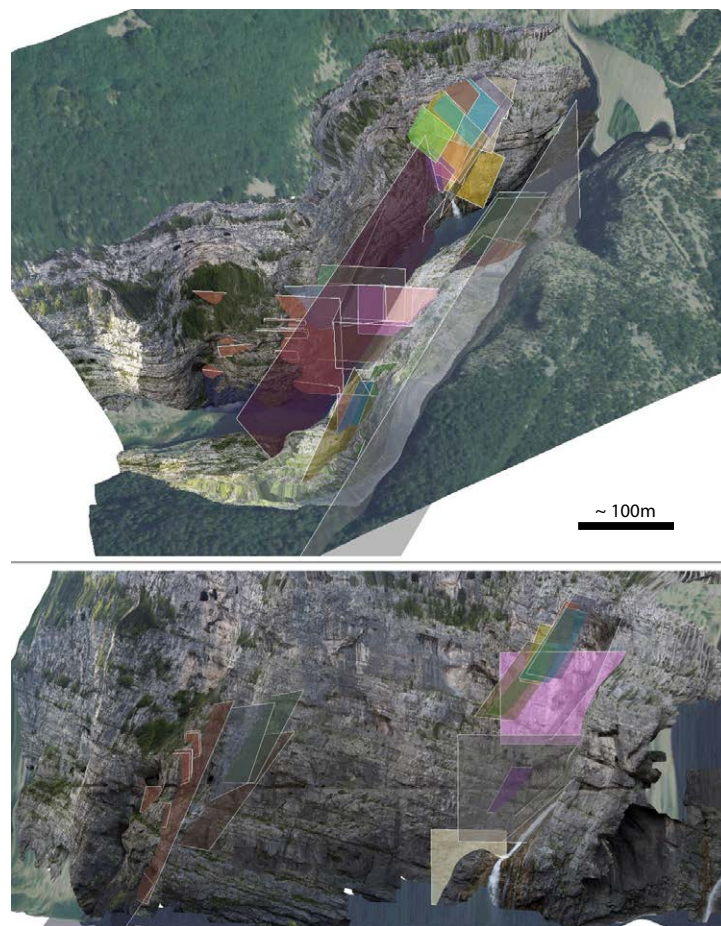
4. The boundaries of dolostone bodies for each scenario were extracted from the tetrahedral volume as lithology = 2 isosurfaces.

5. The isosurfaces were remeshed and slightly smoothed to obtain the final dolostone body boundaries shown in Figure 11.
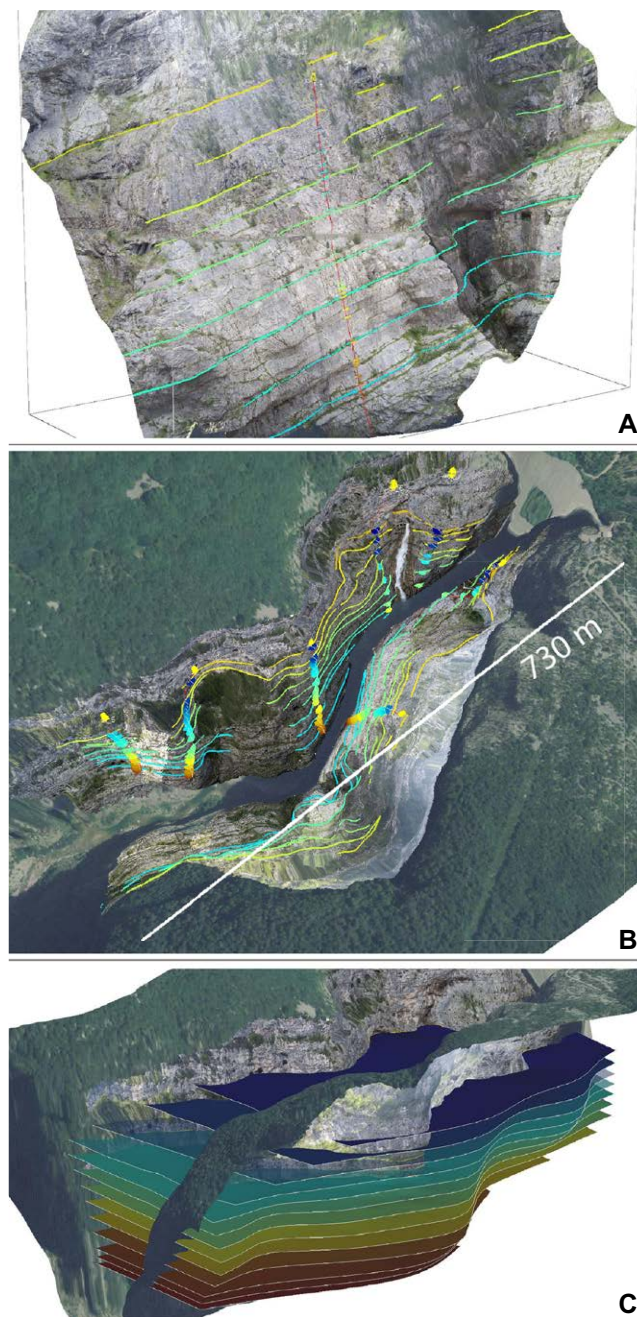
To view the 3D interactive versions of Figures 9 and 10, please visit www.unimib.it/geo3d.

~ 100m

Figure 9. Fault surfaces directly digitized as three-dimensional (3D) rectangular surfaces, based on their traces on the gorge walls. Scale varies in these 3D views. To view the 3D interactive version of Figure 9, please visit www.unimib.it/geo3d.

6. The lithology properties for the minimum, intermediate, and maximum scenarios were transferred directly from the unstructured tetrahedral mesh volume to a regular hexahedral grid (voxet) suitable for exporting dolostone geobodies to different geomodeling packages (Fig. 12).
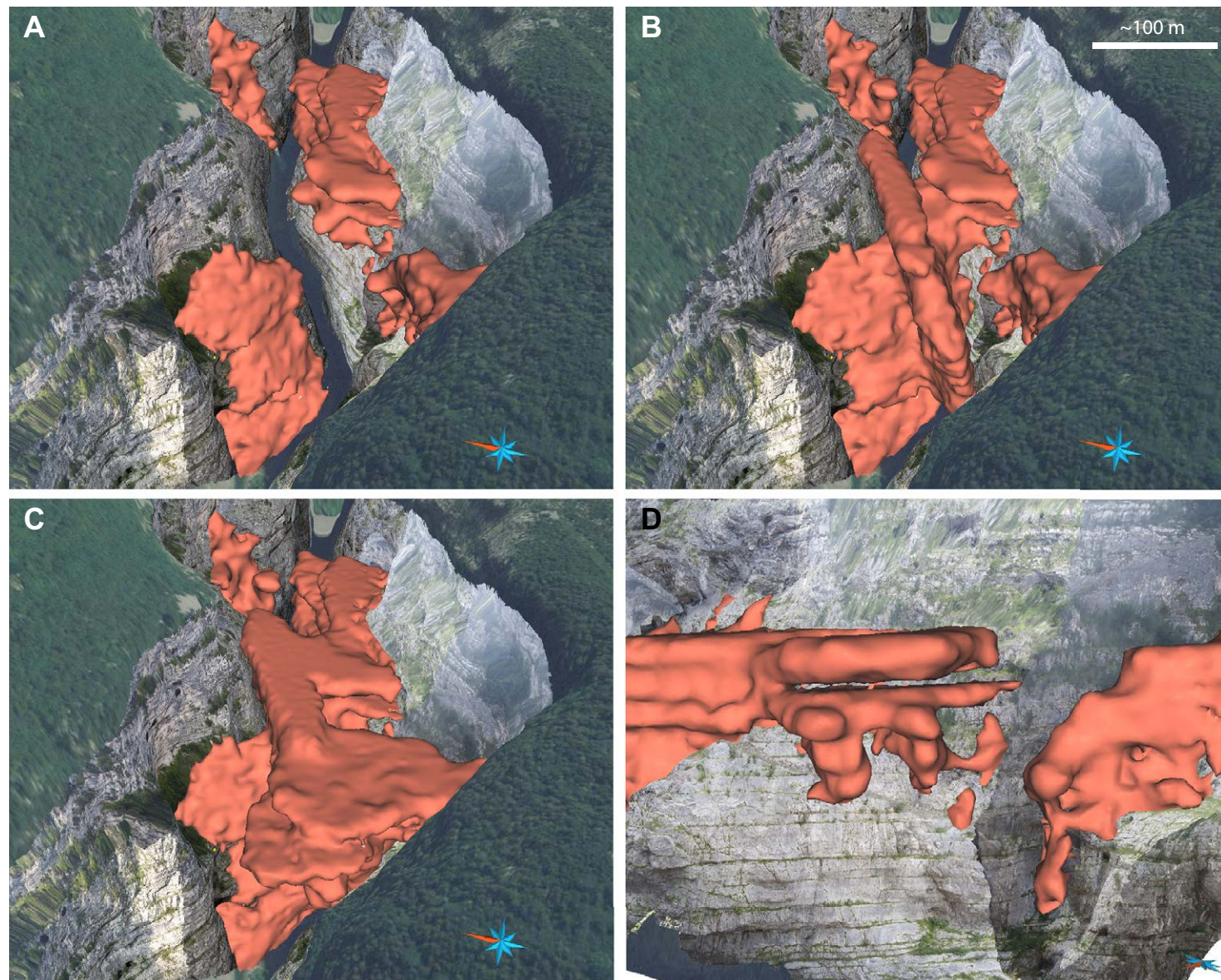
When applied to the same input data and assumptions, the two methodologies tested in this project resulted in similar geometries and almost identical volumes for the dolostone bodies. However, the second methodology is much faster and allows for an easier generation of different scenarios, e.g., changing the dolostone volume just in particular regions of the 3D model. Moreover, in

~100m
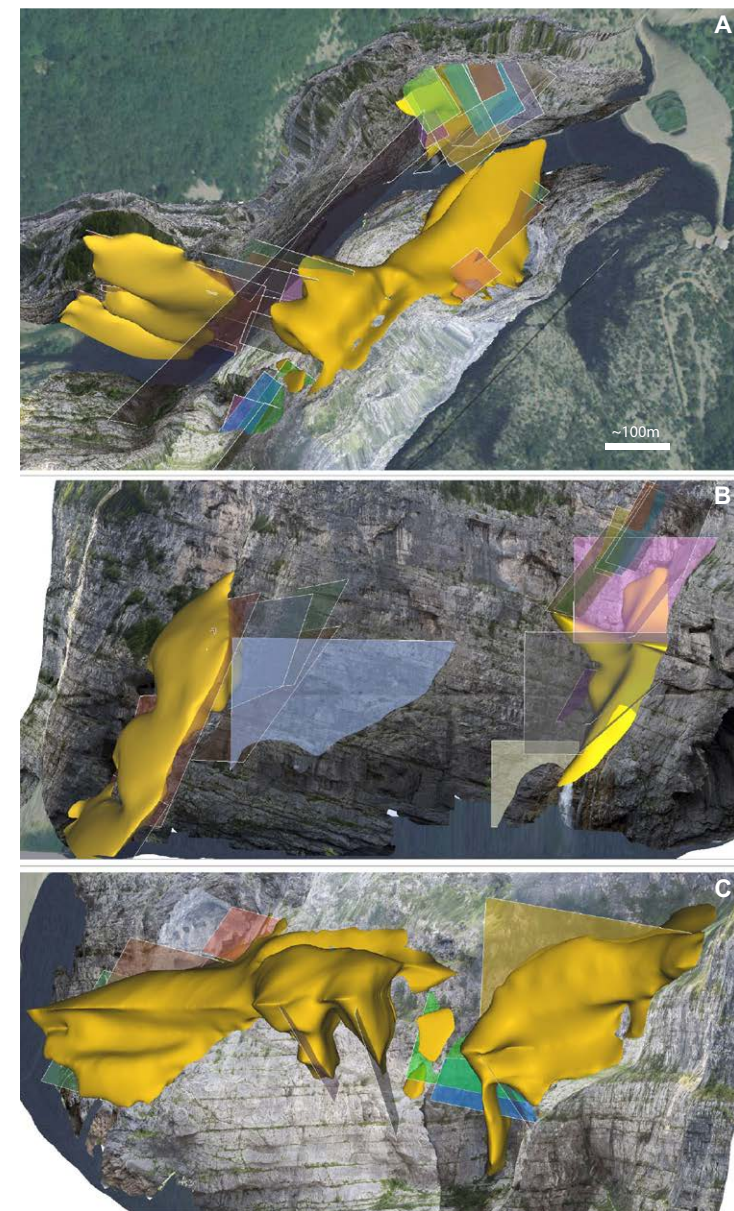
Figure 10. Three-dimensional visualization of model dolostone bodies obtained with workflow A in the Vajont Gorge. (A) Overview from top. (B) North side. (C) South side. The complex geometry and anisotropy of these bodies are assumed to be controlled by faults and bedding. Scale varies in these 3D views. To view the 3D interactive version of Figure 10, please visit www.unimib.it/geo3d.

Bistacchi et al. | Digital outcrop model study of fault-related dolomitization in the Vajont Limestone

To view the 3D interactive version of Figure 11, please visit www.unimib.it/geo3d.

Figure 11. Three-dimensional (3D) visualization of model dolostone bodies obtained with workflow B in the Vajont Gorge. (A) Minimum volume model. (B) Intermediate volume model. (C) Maximum volume model. (D) This workflow allows for detailed modeling of bed-scale heterogeneous dolomitization. Scale varies in these 3D views. To view the 3D interactive version of Figure 11, please visit www.unimib.it/geo3d.
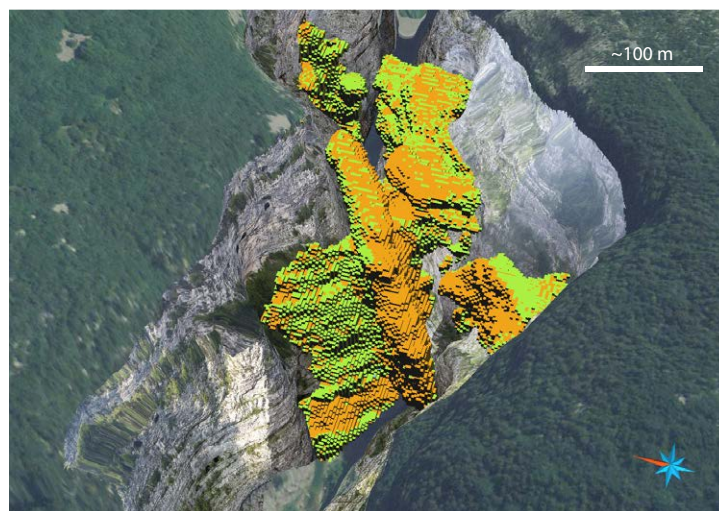
Figure 12. Voxet representation (regular hexahedral grid) of dolostone geobodies suitable for exporting to different geomodeling packages. Scale varies in this three-dimensional view.

the second workflow the output as regular grids (voxets) is more direct. For these reasons the second methodology is preferred and was applied to the final modeling of different scenarios with different facies proportions.

■ 5. DISCUSSION

5.1. Model of Dolomitization in the Vajont Gorge

The approach undertaken in this DOM project, based on photogrammetric data collection and visualization of triangulated surfaces textured with the original full-resolution images, allowed for 3D reconstruction of stratigraphy and structure, and for modeling of the complex geometries of dolostone bodies. This, together with structural observations summarized herein, allowed for construction of an evolutionary model of dolomitization in the Vajont Limestone. The shape of the dolostone bodies, particularly those on the north side of the gorge, suggests that they are controlled by fault zones or fracture corridors since the bodies are generally thin and steeply dipping parallel to fault sets; only in their upper part do the dolostone geobodies seem to extend further from fault zones along bedding, particularly in the fault hanging walls, resulting in asymmetrical mushroom-shaped geometries (Figs. 10 and 11). This is quite different from geometries considered in previous studies, where dome-shaped bodies with a circular shape in map view were postulated (Zempolich and Hardie, 1997).

The dolomitization process, involving a complete replacement of the original limestone, masks most preexisting stratigraphic and structural features. For this reason, it is not possible to directly map the original structures along which fluid flow took place and it is difficult to infer the kinematics of these fault zones. Looking for a strategy to solve this problem, we noted that the dolostone bodies are associated with small, but consistent, changes in attitude of the bedding surfaces. These changes in attitude consistently define a staircase structure with an overall extensional offset along west-northwest- and north-northwest-dipping ghost fault zones aligned with the dolostone bodies, having approximately the same attitude as either the Ext1 or Ext2 extensional fault set. This suggests the inflow of Mg-rich fluids along these fault sets. The offsets associated with these ghost fault zones are revealed by cutting cross sections in the 3D model and are in the 5–10 m range (Fig. 13). Moreover, a high density of extensional fault zones and fractures can be detected in the DOM in limestones cropping out on top of the dolostone bodies. This is particularly evident on the north side of the Vajont Gorge (Fig. 14). Part of these extensional fault zones and fractures predate (at least slightly) dolomitization (Fig. 14). However, other extensional fault zones with cataclastic cores cemented by dolomite (Fig. 2) are present within the dolostone bodies. These cataclasites are composed of dolostone clasts cemented by dolomite and are associated with the extensional deformation, also defined by dolomite veins. Given these mutual crosscutting relationships, dolomitization and the development of extensional fault zones can be considered contemporaneous. Therefore, we propose the following scenario for fault-controlled dolomitization in the Vajont Limestone.

1. After marine phreatic cementation and compaction of the limestones (Zempolich and Hardie, 1997) but before contractional deformations, probably in the Late Jurassic or Cretaceous, extensional tectonics resulted in nucleation and propagation of extensional fault sets (Ext1, Ext2, Ext3), with associated jointing.

2. Extensional damage zones allowed the circulation of Mg-rich fluids, which resulted in dolomitization of the Vajont Limestone, particularly in highly fractured fault tip regions. This might also explain why the observed offsets are very small. The dolomitization of fault-tip zones was not complete, preserving highly fractured limestone sectors on top of the dolostone bodies (Fig. 14). At this stage the dolomitization developed preferentially along layers in the upper hanging-wall section of fault zones (higher fracture density and/or fluid pressure?), resulting in characteristic mushroom-shaped dolostone bodies (Figs. 10 and 11).

3. After the main stage of dolomitization, extensional tectonics continued, leading to the development of late-stage extensional fault zones also within the dolostone bodies, with cataclasites cemented by dolomite and dolomite veins (Fig. 2).

4. During the Tertiary orogenic phases, other fault zones developed (and some of the preexisting fault zones were reactivated), resulting in fault sets RL, LL, Thr1, and Thr2, characterized by calcite cement in both limestones and dolostones. With respect to nearby areas, reactivation was limited in the Vajont Gorge.

To view the 3D interactive version of Figure 14, please visit www.unimib.it/geo3d.
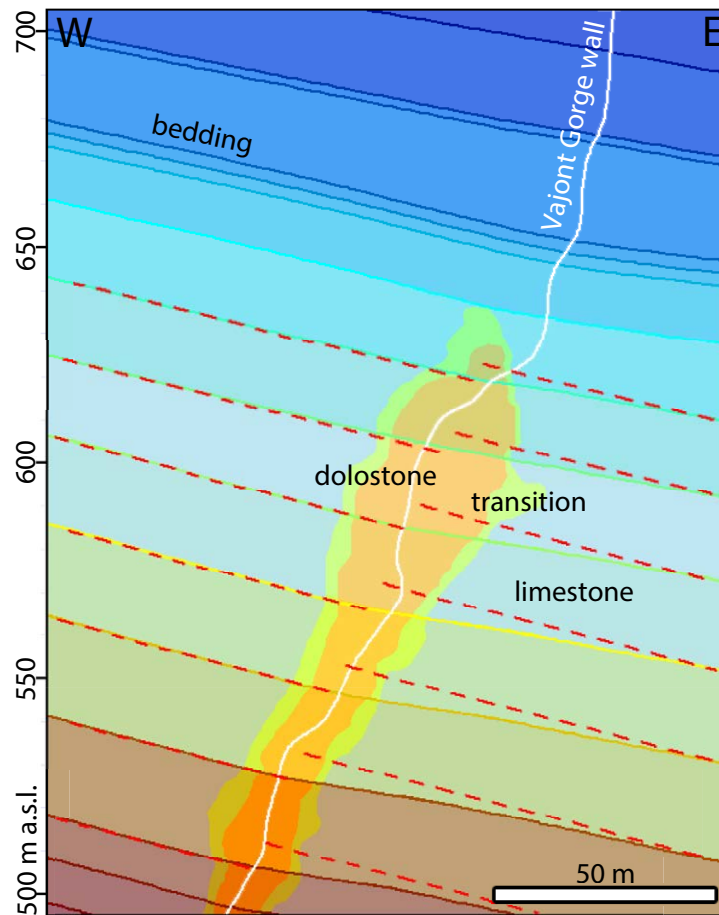
Figure 13. Two-dimensional profile across the dolostone body that crops out in the western sector of the north side of the Vajont Gorge, showing the bend in bedding in the region of the dolostone body, interpreted as separation due to faulting coeval with dolomitization. The profile was extracted using Skua-Gocad tools (see text) from the stratigraphic 3D model, and it is oriented parallel to fault dip and perpendicular to strike in order to evidence dip-slip separations that are more difficult to detect on the oblique outcrop face (white line). Colors represent stratigraphy as in Figure 8C. Red dashed lines highlight the projected separation, which decreases upsection approaching the inferred fault tipline. Orange and yellow represent the dolostone body and the dolostone-limestone transition facies (a.s.l.—above sea level).
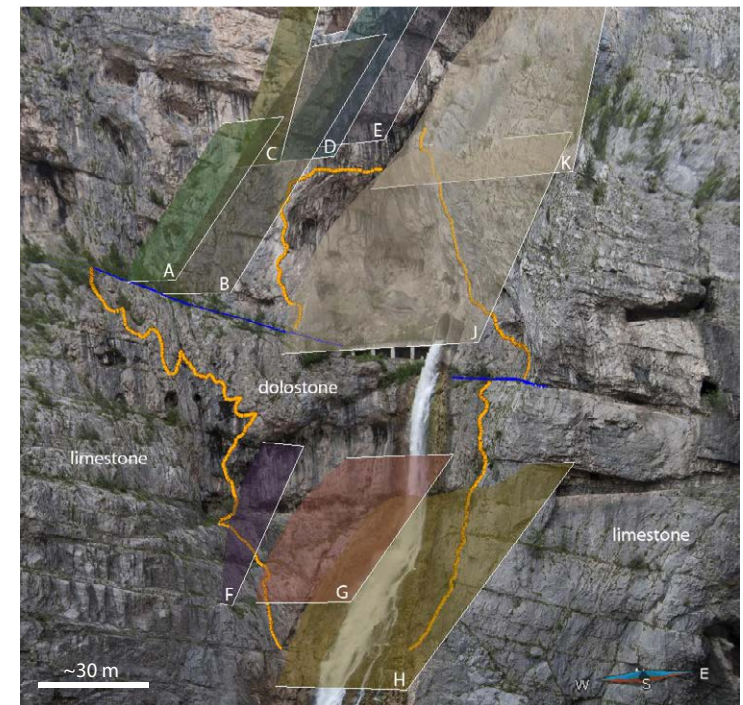

Figure 14. Ext1 and Ext3 faults and fractures occurring just above the dolostone bodies on the northeast side of the Vajont Gorge. Faults A to E predate dolomitization (they are cut by the dolomitization front), while faults F to K postdate dolomitization (they develop both in limestone and dolostone, where they are characterized by cataclasites with dolostone clasts and dolomite cement). Scale varies in this three-dimensional view. To view the 3D interactive version of Figure 14, please visit www.unimib.it/geo3d.

5.2. DOM Methodology

Reconstruction of a high-quality DOM was possible despite the logistic and technical difficulties that were encountered in the Vajont Gorge, highlighting the novelty and utility of the workflows described in this contribution. In the

Vajont Gorge, the geological problem, i.e., the reconstruction of relationships between faulting and dolomitization in originally tight limestones, required the collection of a DOM on almost vertical walls almost 300 m high, along a sinuous gorge more than 700 m long (Fig. 5). The gorge is narrow and sinuous and there is no single point from which a complete view of the walls is possible, so the data set had to necessarily result from a mosaic of data collected from different viewpoints (Fig. 5). The equipment had to be as simple and light as possible to be able to reach some difficult viewpoints. For these reasons, a close-range photogrammetry approach was adopted. Our DOM data set allowed for definition of bedding, lithology (limestone versus dolostone), and fractures and faults, with a spatial resolution at the centimeter scale. Our results contradict Hodgetts (2013, p. 351), who stated "Though cost effective close range photogrammetry works best on scales of up to a few 10's meters, and at the moment is not necessarily a viable alternative for reservoir scale studies." This results

from recent important improvements in algorithms, software, and hardware, and particularly by the possibility offered by SFM photogrammetry to process large and highly redundant collection of photos, where errors are very much reduced because each point in the model is viewed from several photos, and not from just two photos (stereocouple) as in traditional photogrammetry.

In order to exploit the original image data at the highest possible resolution directly in Skua-Gocad, our DOM is composed of multiple triangulated surfaces textured with the original images using a pin-hole projection. This allows for interpretation directly in Skua-Gocad, where the subsequent geological modeling is carried out, and eventually for cross-checking the results of modeling with the image data at high resolution, with obvious advantages both in terms of speed and ease of interpretation and modeling, and in terms of quality checks of the results. We believe that this is a significant advance in DOM-based workflows that traditionally involved two separate phases (e.g., Hodgetts, 2013): (1) interpretation in topography and surveying software, and (2) modeling in geomodeling packages. In fact, breaking the workflow into two steps, performed with different software, does not allow to perform an interactive quality check in the second step (geomodeling), because only the interpretation performed on the DOM, but not the DOM itself, is usually imported in the geomodeling software.

Regarding the reconstruction of triangulated surfaces from the point cloud, we highlight that the Poisson surface reconstruction algorithm (Kazhdan et al., 2006) used in our workflow proved very effective and allowed the problems with Delaunay approaches (evidenced, e.g., by Hodgetts, 2013) to be overcome. In particular, this algorithm results in variable resolution meshes with increased detail where the outcrop surface shows more variability and larger triangles where outcrops are smooth.

Comparing our workflow to others where textured triangulated surfaces are used, we highlight that by using the original images for texturing we obtained a 100-fold increase in resolution with respect to recent contributions. For example, Tavani et al. (2014) textured their outcrop surfaces with a single 16 MB image, obtained by resampling the original photos, while we use 1.2 GB of unresampled images to cover the Vajont Gorge, and if needed we could have increased the resolution in specific regions of the DOM, simply by using a longer focal length lens (Fig. 5).

Finally, we compare photogrammetry and LIDAR workflows. Photogrammetry involves lighter weight and more economic hardware, but one might wonder about the quality of the data. Photogrammetry provides point clouds and perfectly aligned images (point clouds come from images) at an arbitrary resolution, which depends on the distance to the outcrop and the lenses, and can be increased simply using long-focal-length lenses (Fig. 5). Increasing the resolution means increasing the computation time, but this is counterbalanced by the availability of increasingly powerful workstations and efficient algorithms. Powerful workstations and efficient SFM algorithms applied to large photo collections (several hundred to thousands of photos) also solved accuracy problems, and particularly large-scale distortion, common with earlier photogrammetric approaches (e.g., Wu, 2014).

On the other hand, LIDAR provides a well-tested accuracy, which is quoted for each particular instrument (a few centimeters in typical applications). The data set consists of data acquired by the LIDAR instrument (point cloud and intensity of reflection; Hodgetts, 2013), and by a camera attached to the laser scanner, used to obtain a photorealistic data set. In our opinion this is a weak point for two reasons: (1) possible misalignment between LIDAR and camera, and (2) different resolution of the two devices. Alignment between the LIDAR point cloud and photos is generally achieved thanks to a calibration based on reflective targets that can be recognized in both data sets (see e.g., RIEGL RiSCAN manual, www.riegl.com). This calibration takes time and always involves small errors (e.g., Vosselman and Maas, 2010). If the camera is equipped with a wide-angle lens, each pixel covers a relatively large area on the outcrop and the image resolution is lower than the LIDAR resolution, and therefore more than one point in the point cloud shares the same RGB value. In this case the alignment of photos and LIDAR data is less critical, but the combined data set (point cloud plus RGB) shows a relevant decrease in quality. However, high-resolution photos collected with a long-focal-length lens are more difficult to align with the LIDAR point cloud. Generally long-focal-length lenses are not used, and so the real combined (point cloud plus RGB) resolution of LIDAR data sets is generally lower than the nominal point cloud resolution.

5.3. Uncertainty and Alternative Scenarios for 3D Modeling of Irregularly Shaped Geobodies

Reaction fronts or intrusive bodies result in very complex geobodies, with irregular and convolute shapes (Fig. 6); therefore, their modeling is associated with a varying, and sometimes high, degree of uncertainty (Bistacchi et al., 2008). In DOM studies the interpretation is reliable close to the outcrops, but it is progressively less reliable, and increasingly based on prior knowledge of the region, as the distance from outcrop increases. The only volumes where uncertainty is low are those where some information is also available in the subsurface, from boreholes (e.g., Bistacchi et al., 2010), geophysics (e.g., Francese et al., 2009), or, as in the Vajont Gorge case, tunnels. Despite this uncertainty, this kind of reconstruction represents a significant improvement with respect to traditional qualitative field surveys (e.g., Zempolich and Hardie, 1997) for two reasons: (1) the 3D models can be used in further modeling and field studies, and (2) the uncertainty can be visualized and evaluated in 3D.

One possible approach to uncertainty is represented by exploring end-member and intermediate models, all compatible with input data, defined as alternative scenarios. In the Vajont Gorge case, we have generated three scenarios with variable volumes of the dolomitized bodies (minimum, intermediate, and maximum). The dolostone proportion in the volumetric models is 5%, 8%, and 11% (minimum, intermediate, and maximum scenarios, respectively; Table 2). An attempt at generating a scenario with an even higher dolostone proportion was done, but was unsuccessful as it is not possible to model more dolostone in the gorge given the constraint of the outcrops.

TABLE 2. FACIES PROPORTION IN THE THREE-DIMENSIONAL MODEL
FOR THE MINIMUM, INTERMEDIATE, AND MAXIMUM SCENARIOS

Scenarios	Facies	Volume (m^3)	Proportion (%)
minimum	total	57,128,956	100.00
	dolostone	2,838,610	4.97
	limestone	54,290,400	95.03
intermediate	total	57,128,956	100.00
	dolostone	4,612,610	8.07
	limestone	52,516,400	91.93
maximum	total	57,128,956	100.00
	dolostone	6,311,370	11.05
	limestone	50,817,600	88.95

The areal facies proportion measured on the north and south walls of the Vajont Gorge are 11% and 10%, respectively (Table 1). Only in the maximum scenario is the volumetric facies proportion the same as the areal one, while in the other two scenarios the volumetric dolostone proportion is 2/3 and 1/2 with respect to the areal proportion. We infer that the difference in 2D and 3D facies proportion is possibly a result of differential erosion of dolostone and limestone in the gorge. In other words, due to heterogeneous and anisotropic distribution of dolostone, and due to preferential erosion, the areal facies proportion is not necessarily representative of the volumetric facies proportion. This is one of the reasons why this 3D study represents an improvement with respect to traditional 2D studies.

■ 6. CONCLUSIONS

We presented the results of a photogrammetric study of the Vajont Gorge, in the eastern Dolomites, Southern Alps, Italy. The DOM approach in this work is innovative for three principal reasons: (1) data were generated with SFM photogrammetry (close range photogrammetry, never performed before in DOM studies at this scale), (2) visualization is based on triangulated surfaces textured with the original full-resolution images (never done before), and (3) DOM data were interpreted directly in a geomodeling package (Gocad), resulting in a seamless workflow from DOM interpretation to modeling (never implemented before).

This workflow results in a much higher resolution data set with respect to any previous achievement developed with photogrammetry (e.g., Tavani et al., 2014) or LIDAR (e.g., Hodgetts, 2013) over a similar volume.

Another relevant difference with previous projects is that we are able to perform the interpretation directly in Skua-Gocad, while others performed it in external software and then imported the results in geomodeling packages (e.g., Tavani et al., 2014; Hodgetts, 2013).

The 3D geological model developed in this study points to a dolomitization scenario in the Vajont Limestone, where Mg-rich fluid flow was controlled by Mesozoic extensional fault zones, in contrast with previous interpretations, based on field work carried out with only traditional techniques, suggesting a late fluid circulation along Tertiary thrust faults (Zempolich and Hardie, 1997).

REFERENCES CITED

Bellian, J.A., 2005, Digital outcrop models: Applications of terrestrial scanning lidar technology in stratigraphic modeling: Journal of Sedimentary Research, v. 75, p. 166–176, doi:10.2110/jsr.2005.013.

Bistacchi, A., Massironi, M., Dal Piaz, G.V., Dal Piaz, G., Monopoli, B., Schiavo, A., and Toffolon, G., 2008, 3D fold and fault reconstruction with an uncertainty model: An example from an Alpine tunnel case study: Computers & Geosciences, v. 34, p. 351–372, doi:10.1016/j.cageo.2007.04.002.

Bistacchi, A., Massironi, M., and Menegon, L., 2010, Three-dimensional characterization of a crustal-scale fault zone: The Pusteria and Sprechenstein fault system (Eastern Alps): Journal of Structural Geology, v. 32, p. 2022–2041, doi:10.1016/j.jsg.2010.06.003.

Bistacchi, A., Ashley Griffith, W., Smith, S.A.F., di Toro, G., Jones, R.R., and Nielsen, S., 2011, Fault roughness at seismogenic depths from LIDAR and photogrammetric analysis: Pure and Applied Geophysics, v. 168, p. 2345–2363, doi:10.1007/s00024-011-0301-7.

Bistacchi, A., Mittempergher, S., Smith, S.A.F., Di Toro, G., Mitchell, T., and Nielsen, S., 2013, Towards measuring large-scale hydraulic properties of the seismogenic Gole Larghe fault zone at 8 km depth: European Geosciences Union General Assembly 2013, abs. EGU2013–10335.

Bosellini, A., and Masetti, D., 1972, Ambiente e dinamica deposizionale del Calcare del Vajont (Giurassico medio, Prealpi Bellunesi e Friulane): Annali dell'Università di Ferrara (Sezione Scienze Geologiche e Paleontologiche), v. 5, p. 87–100.

Buckley, S.J., Howell, J.A., Enge, H.D., and Kurz, T.H., 2008, Terrestrial laser scanning in geology: Data acquisition, processing and accuracy considerations: Journal of the Geological Society, London, v. 165, p. 625–638, doi:10.1144/0016-76492007-100.

Candela, T., Renard, F., Bouchon, M., Brouste, A., Marsan, D., Schmittbuhl, J., and Voisin, C., 2009, Characterization of fault roughness at various scales: Implications of three-dimensional high resolution topography measurements: Pure and Applied Geophysics, v. 166, p. 1817–1851, doi:10.1007/s00024-009-0521-2.

Castellarin, A., and Cantelli, L., 2000, Neo-Alpine evolution of the southern Eastern Alps: Journal of Geodynamics, v. 30, p. 251–274, doi:10.1016/S0264-3707(99)00036-8.

Chistolini, F., Bistacchi, A., Massironi, M., Consonni, D., and Cortinovis, S., 2014, Polyphase tertiary fold-and-thrust tectonics in the Belluno Dolomites: New mapping, kinematic analysis, and 3D modelling: European Geosciences Union General Assembly 2014, abs. EGU2014–14192.

Dal Piaz, G.V., Bistacchi, A., and Massironi, M., 2003, Geological outline of the Alps: Episodes, v. 26, p. 175–180.

Doglioni, C., 1990, Thrust tectonics examples from the Venetian Alps: Studi Geologici Camerti, special volume, p. 117–129.

Doglioni, C., 1992a, Relationships between mesozoic extensional tectonics, stratigraphy and Alpine inversion in the Southern Alps: Eclogae Geologicae Helvetiae, v. 85, p. 105–126.

Doglioni, C., 1992b, The Venetian Alps thrust belt, in McClay, K.R., ed., Thrust tectonics: London, Springer, p. 319–324.

Dueholm, K.S., and Olsen, T., 1993, Reservoir analog studies using multimodel photogrammetry: A new tool for the petroleum industry: American Association of Petroleum Geologists Bulletin, v. 77, p. 2023–2031.

Ferasin, F., 1956, Geologia dei dintorni di Cimolais (Udine): Memorie degli Istituti di Geologia e Mineralogia dell'Università di Padova, v. 20, p. 1–32.

Francese, R., Mazzarini, F., Bistacchi, A., Morelli, G., Pasquarè, G., Praticelli, N., Robain, H., Wardell, N., and Zaja, A., 2009, A structural and geophysical approach to the study of fractured aquifers in the Scansano-Magliano in Toscana Ridge, southern Tuscany, Italy: Hydrogeology Journal, v. 17, p. 1233–1246, doi:10.1007/s10040-009-0435-1.

Frank, T., Tertois, A.-L., and Mallet, J.-L., 2007, 3D-reconstruction of complex geological interfaces from irregularly distributed and noisy point data: Computers & Geosciences, v. 33, p. 932–943, doi:10.1016/j.cageo.2006.11.014.

Furukawa, Y., and Ponce, J., 2010, Accurate, dense, and robust multiview stereopsis: IEEE Transactions on Pattern Analysis and Machine Intelligence, v. 32, p. 1362–1376, doi:10.1109/TPAMI.2009.161.

Haneberg, W.C., 2008, Using close range terrestrial digital photogrammetry for 3-D rock slope modeling and discontinuity mapping in the United States: Bulletin of Engineering Geology and the Environment, v. 67, p. 457–469, doi:10.1007/s10064-008-0157-y.

Hartley, R.I., and Zisserman, A., 2004, Multiple view geometry in computer vision (second edition): Cambridge, UK, Cambridge University Press, 670 p.

Hodgetts, D., 2013, Laser scanning and digital outcrop geology in the petroleum industry: A review: Marine and Petroleum Geology, v. 46, p. 335–354, doi:10.1016/j.marpetgeo.2013.02.014.

Kazhdan, M., Bolitho, M., and Hoppe, H., 2006, Poisson surface reconstruction, in Polthier, K., and Sheffer, A., eds., Eurographics Symposium on Geometry Processing 2006: Aire-la-Ville, Switzerland, Eurographics Association, p. 1–10.

Kurz, T.H., Dewit, J., Buckley, S.J., Thurmond, J.B., Hunt, D.W., and Swennen, R., 2012, Hyperspectral image analysis of different carbonate lithologies (limestone, karst and hydrothermal dolomites): The Pozalagua Quarry case study (Cantabria, northwest Spain): Sedimentology, v. 59, p. 623–645, doi:10.1111/j.1365-3091.2011.01269.x.

Lebel, D., Vuitton, R., Masse, L., Deblonde, C., Kirkwood, D., Marcil, J.S., Vallé, M.A., Da Roza, R., and Malo, M., 2001, Integration of photogrammetric data in the construction of a 3-D geological model in a thrust-fold belt, Moose Mountain, Alberta, Canada: Journal of the Virtual Explorer, v. 4, p. 6, doi:10.3809/jvirtex.2001.00033.

Lillesand, T.M., Kiefer, R.W., and Chipman, J.W., 2008, Remote sensing and image interpretation (sixth edition): Hoboken, New Jersey, John Wiley, 804 p.

Lovely, P., Zahasky, C., and Pollard, D.D., 2010, Fold geometry at Sheep Mountain anticline, Wyoming, constructed using airborne laser swath mapping data, outcrop-scale geologic mapping, and numerical interpolation: Journal of Geophysical Research, v. 115, B12414, doi:10.1029/2010JB007650.

Maerten, L., Pollard, D.D., and Maerten, F., 2001, Digital mapping of three-dimensional structures of the Chimney Rock fault system, central Utah: Journal of Structural Geology, v. 23, p. 585–592, doi:10.1016/S0191-8141(00)00142-5.

Mallet, J.-L., 2002, Geomodeling: New York, Oxford University Press, 624 p.

Masetti, D., Fantoni, R., Romano, R., Sartorio, D., and Trevisani, E., 2012, Tectonostratigraphic evolution of the Jurassic extensional basins of the eastern southern Alps and Adriatic foreland based on an integrated study of surface and subsurface data: American Association of Petroleum Geologists Bulletin, v. 96, p. 2065–2089, doi:10.1306/03091211087.

Massironi, M., Zampieri, D., Superchi, L., Bistacchi, A., Ravagnan, R., Bergamo, A., Ghirotti, M., and Genevois, R., 2013, Geological structures of the Vajont landslide: Italian Journal of Engineering Geology and Environment, v. 2013, p. 573–582, doi:10.4408/IJEGE.2013-06.B-55.

McCaffrey, K.J.W., Jones, R.R., Holdsworth, R.E., Wilson, R.W., Clegg, P., Imber, J., Holliman, N., and Trinks, I., 2005, Unlocking the spatial dimension: Digital technologies and the future of geoscience fieldwork: Journal of the Geological Society, London, v. 162, p. 927–938, doi:10.1144/0016-764905-017.

Pearce, M.A., Jones, R.R., Smith, S.A.F., McCaffrey, K.J.W., and Clegg, P., 2006, Numerical analysis of fold curvature using data acquired by high-precision GPS: Journal of Structural Geology, v. 28, p. 1640–1646, doi:10.1016/j.jsg.2006.05.010.

Pennacchioni, G., and Mancktelow, N.S., 2007, Nucleation and initial growth of a shear zone network within compositionally and structurally heterogeneous granitoids under amphibolite facies conditions: Journal of Structural Geology, v. 29, p. 1757–1780, doi:10.1016/j.jsg.2007.06.002.

Riva, M., Besio, M., Masetti, D., Roccati, F., Sapigni, M., and Semenza, E., 1990, Geologia delle Valli Vaiont e Gallina (Dolomiti orientali): Annali dell'Università di Ferrara, v. 2, p. 55–76.

Ronchi, P., Masetti, D., Tassan, S., and Camocino, D., 2012, Hydrothermal dolomitization in platform and basin carbonate successions during thrusting: A hydrocarbon reservoir analogue (Mesozoic of Venetian Southern Alps, Italy): Marine and Petroleum Geology, v. 29, p. 68–89, doi:10.1016/j.marpetgeo.2011.09.004.

Smith, S.A.F., Bistacchi, A., Mitchell, T.M., Mittempergher, S., and Di Toro, G., 2013, The structure of an exhumed intraplate seismogenic fault in crystalline basement: Tectonophysics, v. 599, p. 29–44, doi:10.1016/j.tecto.2013.03.031.

Snavely, N., Seitz, S.M., and Szeliski, R., 2006, Photo tourism: Exploring photo collections in 3D, in SIGGRAPH Conference Proceedings: New York, ACM Press, p. 835–846.

Tavani, S., Granado, P., Corradetti, A., Girundo, M., Iannace, A., Arbués, P., Muñoz, J.A., and Mazzoli, S., 2014, Building a virtual outcrop, extracting geological information from it, and sharing the results in Google Earth via OpenPlot and Photoscan: An example from the Khaviz Anticline (Iran): Computers & Geosciences, v. 63, p. 44–53, doi:10.1016/j.cageo.2013.10.013.

Trinks, I., Clegg, P., McCaffrey, K.J.W., Jones, R.R., Hobbs, R., Holdsworth, B., Holliman, N., Imber, J., Waggott, S., and Wilson, R., 2005, Mapping and analysing virtual outcrops: Visual Geosciences, v. 10, p. 13–19, doi:10.1007/s10069-005-0026-9.

Tsai, R.Y., 1987, A versatile camera calibration technique for high-accuracy 3D machine vision metrology using off-the-shelf TV cameras and lenses: IEEE Journal on Robotics and Automation, v. RA-3, p. 323–344, doi:10.1109/JRA.1987.1087109.

Vasuki, Y., Holden, E.J., Kovesi, P., and Micklethwaite, S., 2014, Semi-automatic mapping of geological structures using UAV-based photogrammetric data: An image analysis approach: Computers & Geosciences, v. 69, p. 22–32, doi:10.1016/j.cageo.2014.04.012.

Vosselman, G., and Maas, H.-G., 2010, Airborne and terrestrial laser scanning: Dunbeath, UK, Whittles Publishing, 336 p.

White, P.D., and Jones, R.R., 2008, A cost-efficient solution to true color terrestrial laser scanning: Geosphere, v. 4, p. 564–575, doi:10.1130/GES00155.1.

Wu, C., 2013, Towards linear-time incremental structure from motion, in Proceedings, 2013 International Conference on 3D Vision, 3DV 2013: Seattle, Washington, Institute of Electrical and Electronics Engineers, p. 127–134, doi:10.1109/3DV.2013.25.

Wu, C., 2014, Critical configurations for radial distortion self-calibration, in Proceedings, 2014 IEEE Conference on Vision and Pattern Recognition (CVPR): Piscataway, New Jersey, Institute of Electrical and Electronics Engineers, p. 25–32, doi:10.1109/CVPR.2014.11.

Xu, X., Bhattacharya, J.B., Davies, R.K., and Aiken, C.L.V., 2001, Digital geologic mapping of the Ferron Sandstone, Muddy Creek, Utah, with GPS and reflectorless laser rangefinders: GPS Solutions, v. 5, p. 15–23, doi:10.1007/PL00012872.

Zempolich, W.G., and Hardie, L.A., 1997, Geometry of dolomite bodies within deep-water resedimented oolite of the Middle Jurassic Vajont Limestone, Venetian Alps, Italy: Analogs for hydrocarbon reservoirs created through fault-related burial dolomitization, in Kupecz, J., et al., eds., Reservoir quality prediction in sandstones and carbonates: An overview: American Association of Petroleum Geologists Memoir 69, p. 127–162.